A vibro-impact acoustic black hole for passive damping of flexural beam vibrations

Haiqin Li, Cyril Touzé, Adrien Pelat, François Gautier, Xianren Kong

▶ **To cite this version:**

Haiqin Li, Cyril Touzé, Adrien Pelat, François Gautier, Xianren Kong. A vibro-impact acoustic black hole for passive damping of flexural beam vibrations. Journal of Sound and Vibration, 2019, 450, pp.28-46. 10.1016/j.jsv.2019.03.004 . hal-02086389

HAL Id: hal-02086389
https://hal.science/hal-02086389

Submitted on 1 Apr 2019

HAL is a multi-disciplinary open access archive for the deposit and dissemination of scientific research documents, whether they are published or not. The documents may come from teaching and research institutions in France or abroad, or from public or private research centers.

L'archive ouverte pluridisciplinaire **HAL**, est destinée au dépôt et à la diffusion de documents scientifiques de niveau recherche, publiés ou non, émanant des établissements d'enseignement et de recherche français ou étrangers, des laboratoires publics ou privés.

A vibro-impact acoustic black hole for passive damping of flexural beam vibrations

Haiqin Li[a,b,*], Cyril Touzé[b], Adrien Pelat[c], François Gautier[c], Xianren Kong[a]

[a] *Research Center of Satellite Technology, Harbin Institute of Technology, Harbin 150001, China*
[b] *IMSIA, ENSTA ParisTech-CNRS-EDF-CEA, Université Paris Saclay, 828 Boulevard des Maréchaux, 91762 Palaiseau Cedex, France*
[c] *Laboratoire d'Acoustique de l'Université du Mans, UMR CNRS 6613, Avenue Olivier Messiaen, 72085 Le Mans, Cedex 09, France*

Abstract

Nonlinear flexural vibrations of slender beams holding both an Acoustic Black Hole termination and a contact non-linearity are numerically studied. The Acoustic Black Hole (ABH) effect is a passive vibration mitigation technique, which has shown attractive properties above a given cut-on frequency. In this contribution, a vibro-impact acoustic black hole (VI-ABH) is introduced, the contact nonlinearity being used as a mean to transfer energy from low to high frequencies. A numerical model of a VI-ABH is derived from an Euler-Bernoulli beam. The contact law is handled with a penalization approach, the visco-elastic layer with a Ross-Kerwin-Ungard model and the problem is solved with a modal approach combined with an energy-conserving time integration scheme. Numerical results show that the VI-ABH brings about important modifications, and changes the nature of more traditional black holes, by redistributing all the vibrational energy. It can lead to a strong decrease of the resonance magnitude at low frequencies. Under steady state noise excitation, parametric studies are realised in the cases of a single contact, a grid of contacts and bilateral contacts layouts, in order to find some optimal designs. Transient dynamics is also studied through the analysis of displacement signal envelope and energy decay time. All the numerical results constantly show that the combination the ABH effect and an energy transfer provided by contact nonlinearity leads to very attractive mitigation template including low frequencies.

Keywords:
Flexural vibration mitigation; Damping; Acoustic Black Hole effect; Contact nonlinearity; Energy transfer

1. Introduction

Effective reduction of unwanted vibrations for mechanical structures such as beams and plates represents an important concern in various industrial applications. Classical methods

*Corresponding author.
Email address: lihaiqin1992@yahoo.com (Haiqin Li)

for passive vibration damping generally consist in the use of heavy damping layer [1] or tuned mass dampers [2–4]. These methods have been widely studied and proved to be efficient, but their implementation also result in a strong added mass which are detrimental in many fields from transportation industry to aerospace engineering. Therefore, the development of vibration mitigation techniques without added mass is clearly of interest.

The Acoustic Black Hole (ABH) effect is a passive technique for mitigating vibrations based on the propagation properties of flexural waves in thin structures of variable thickness. Its usual implementation for a beam end consists in smoothly decreasing the thickness by following a power-law profile [5], and coating the thin zone with a viscoelastic layer [6]. The local inhomogeneity of complex stiffness leads to a strong vibration field trapping in the tapered area and induces a particularly effective mitigation of the vibration energy above a threshold frequency that depends on the ABH relative size as compared to the wavelength. As a result, excluding low frequencies, the reflection coefficient of the beam end is very small and the beam displays a non resonant response, as if being of infinite extension.

Theoretical and numerical works have been realised to model the reflection coefficient of ABH beam termination [7, 8], to study the increase of modal damping ratios and modal overlap factor [9], and to optimize the design of ABH structures and its damping layer [10–13], including new shapes of ABH such as spiral [14] or distributions of ABHs embedded in plate-like structures [15]. Other studies consider the ABH effect as a mean for energy harvesting [16]. Experimental evidence of ABH effect using a variety of beam-like and plate-like structures are also numerous [10, 17–21]. All these studies have confirmed the high efficiency of ABH for vibration damping. However, a known and constant drawback of any implementation is that ABH are generally inefficient in the low-frequency range [9, 15]. As a rigorous explanation, a cut-on frequency exists, below which the ABH may lose its effectiveness [22]. Although the cut-on frequency may somehow be reduced by modifying the characteristic parameters of an ABH, it is still unfortunately unavoidable in the traditional linear framework of ABH design.

To improve its overall efficiency in mitigating vibrations, the ABH effect should be advantageously associated with another effect able to address low frequencies. The idea of using a nonlinear mechanism to transfer energy from low frequencies - where the black hole is ineffective - to high frequencies - where the black hole is very efficient, has emerged recently. Geometric nonlinearity as a mean to realize this transfer has been successfully studied in a previous work [23]. However, the time scale of this mechanism is large as compared to typical periods of the targeted low frequency waves, so that the expected gains remain limited and cannot be obtained immediately.

The aim of this work is to use a vibro-impact as nonlinear mechanism to rapidly transfer energy to the high frequency range, in order to improve the efficacy of acoustic black holes. More recently, vibro-impacts have been used in a number of studies concerned with the concept of Nonlinear Energy Sink (NES), defined as nonlinear vibration absorber having no linear restoring force. As shown *e.g.* in [24–26], an NES is able to transfer energy in an irreversible fashion from a primary structure to the attached device. In order to realize the needed *essential* nonlinearity (*i.e.* without linear term), the idea of using vibro-impacts has

been used theoretically and experimentally [27–31]. However, using contact nonlinearity as a mean to transfer energy and damp vibrations of structures with an added acoustic black hole effect, has never been reported, to the authors' knowledge. As it will be underlined in the course of the present paper, the vibro-impact brings about strong modification of the nature of the ABH itself, transforming a linear mechanism to a strongly nonlinear one, and redistributing energy among all frequencies. As a very important change in the damping mechanism itself is proposed, it has been decided to name this new device as VI-ABH for vibro-impact acoustic black hole.

The article presents a numerical investigation of the nonlinear behaviour of such a VI-ABH. It is composed of two main sections. In Section 2, a numerical model is detailed. A special attention is paid to taking into account the variable thickness, to the modeling of the added viscoelastic layer (section 2.2) and the contact points (section 2.3). The numerical scheme for the time integration is detailed in sections 2.4 and 2.5. In a second part, the numerical results are presented and discussed. The beam design is reported in section 3.1, then a convergence study is highlighted (section 3.2). Section 3.3 considers the case of a single contact points, while multiple contacts (section 3.4) layouts are further investigated. Finally, the behaviour of the VI-ABH in transient dynamics is investigated in section 3.6.

2. Numerical modeling of a vibro-impact acoustic black hole

In this section a model of vibro-impact acoustic black hole (VI-ABH) is developed. A VI-ABH consists in a classical ABH in interaction with a rigid barrier via several contact points, as shown in Fig. 1. The dynamics of a beam with variable thickness is first recalled. The modeling of damping induced by the viscoelastic layer and the collision mechanism are then detailed. Finally the numerical method combining a modal approach computed with a finite-difference scheme, and an energy-conserving scheme for time integration, is explained.

2.1. Statement of the problem

The flexural vibrations of an ABH beam of length L and width b in contact with a discrete set of points is considered. Fig. 1 shows the layout of the system, characterized by the black hole profile and its wedge power-law for $x \in [x_{abh}, L]$, and a number of N_c contact points located below the beam, at $x = x_{ci}$ for $i = 1, ...N_c$, where the ABH can impact during its vibration. The location of the contact points can be controlled horizontally and vertically by adjusting the gap h_c. The thickness $h_b(x)$ of the beam depends on the spatial variable x only, following the power-law

$$h_b(x) = \begin{cases} h_0, & \text{for } \; x \in [0, x_{abh}] \\ h_0 \left(\dfrac{x - x_{end}}{x_{abh} - x_{end}} \right)^2, & \text{for } \; x \in [x_{abh}, L] \end{cases} \tag{1}$$

For such an ABH beam, the area of the cross-section $A(x)$ and the inertia moment $I(x)$ respectively reads $A(x) = bh_b(x)$ and $I(x) = bh_b(x)^3/12$.

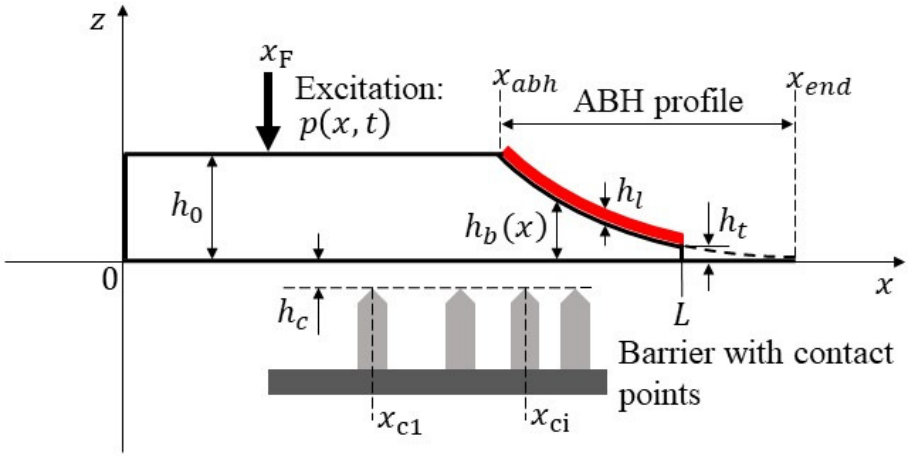

Fig. 1. General layout a VI-ABH composed of an ABH beam in contact with a barrier having a set of discrete contact points. L is the total length of the beam, h_0, $h_b(x)$ and h_t are the thickness of the beam respectively in its uniform area, in the ABH profile, and in the truncated termination, while h_l is the thickness of the damping layer.

Let $u(x,t)$ denote the transverse displacement of the beam. In the framework of Euler-Bernoulli theory for flexural vibration of beams, the equation governing the transverse vibrations writes [32, 33]

$$\rho(x)A(x)\frac{\partial^2 u}{\partial t^2} + \frac{\partial^2}{\partial x^2}\left(D(x)\frac{\partial^2 u}{\partial x^2}\right) = p(x,t) + f(x,t). \tag{2}$$

where $D(x) = E(x)I(x)$ is the bending stiffness, $p(x,t)$ represents the external excitation force located at $x = x_F$, and $f(x,t)$ stands for the contact force exerted by the barrier on the beam when the contact is activated. In a usual configuration of an ABH beam as shown in Fig. 1, a viscoelastic layer is added in order to improve locally the damping capacity of the device. Consequently the local mass density $\rho(x)$ and bending stiffness $D(x)$ are space dependent, they will be subsequently modified in order to take into account the added viscoelastic layer, see Section 2.2.

Finally the beam is assumed to be clamped in $x = 0$ and free in $x = L$ so that the boundary conditions read:

$$\forall\, t,\quad u(0,t) = 0,\quad \left.\frac{\partial u}{\partial x}\right|_{x=0,t} = 0,\quad \left.\frac{\partial^2 u}{\partial x^2}\right|_{x=L,t} = 0,\quad \left.\frac{\partial^3 u}{\partial x^3}\right|_{x=L,t} = 0. \tag{3}$$

The next subsection is devoted to the losses modeling.

2.2. Modeling of added viscoelastic layer: formulation in the frequency domain

The damping properties of ABH are usually obtained by adding a viscoelastic layer of thickness h_l on the wedge profile, as shown in Fig. 1. The effect of this viscoelastic layer can be taken into consideration by using the Ross-Ungar-Kerwin model [1, 23], which

proposes an expression of the complex bending stiffness $D^*(x)$, where $()^*$ refers to the complex representation of the term. For an added viscoelastic layer located in the interval $[x_{abh}, L]$, the complex bending stiffness $D^*(x)$ writes

$$D^*(x) = \begin{cases} E_b I_b(x)\left(1 + j\eta_b\right), & \forall x \in [0, x_{abh}], \\ E_b I_b(x) \left[\left(1 + j\eta_b\right) + \dfrac{E_l}{E_b}\left(\dfrac{h_l}{h_b(x)}\right)^3 \left(1 + j\eta_l\right) + \right. & \\ \left. \dfrac{3\left(1 + \frac{h_l}{h_b(x)}\right)^2 \frac{E_l h_l}{E_b h_b(x)} \left(1 - \eta_b\eta_l + j\left(\eta_b + \eta_l\right)\right)}{1 + \frac{E_l h_l}{E_b h_b(x)}\left(1 + j\eta_l\right)} \right], & \forall x \in [x_{abh}, L], \end{cases} \tag{4}$$

where j is the imaginary unit, E_b, I_b, and η_b are the bending stiffness, the Young modulus, the moment of inertia and the loss factor of the beam alone, while E_l and η_l corresponds to the Young modulus and the loss factor of the viscoelastic layer. The real bending stiffness is simply obtained by taking the real part of the previous expression as $D(x) = \mathrm{Re}\left(D^*(x)\right)$.

The added mass due to the presence of the damping layer is considered via the following equivalent mass density,

$$\rho(x) = \begin{cases} \rho_b, & \forall x \in [0, x_{abh}], \\ \dfrac{\rho_b h_b(x) + \rho_l h_l}{h_b(x) + h_l}, & \forall x \in [x_{abh}, L], \end{cases} \tag{5}$$

where ρ_b and ρ_l stand respectively for the mass densities of the ABH beam and the damping layer. The total thickness of the beam is also modified by the presence of the layer and reads

$$h(x) = \begin{cases} h_b(x), & \forall x \in [0, x_{abh}], \\ h_b(x) + h_l, & \forall x \in [x_{abh}, L]. \end{cases} \tag{6}$$

2.3. Contact force modeling

The collisions between the barrier and the beam are assumed to be pointwise at the abscissas x_{ci}, $i = 1, ..., N_c$ of the contact points. The contact force $f(x,t)$ must describe the strong, local, nonsmooth repelling force acting on the beam each time the gap between the vertical position of the beam and a contact point vanishes. In this contribution, a penalty approach is adopted to describe . Let $g(x)$ represents the vertical location of the contact points and $\eta(x,t) = g(x) - u(x,t)$ the distance between the beam and the unilateral constraint imposed by the contact points. Following [34–36], a repelling force of Hertz-like type can describe the contact as

$$f(x,t) = K_c \left[\eta(x,t)\right]_+^\alpha, \tag{7}$$

where $[\eta]_+ = \frac{1}{2}\left(\eta + |\eta|\right)$. The notation $[\eta]_+$ is used to represent the positive part of η. The contact force vanishes when $\eta < 0$ and takes the power-law form as soon as an interpenetration occurs. The description of the contact force depends on a stiffness parameter $K_c \geq 0$

in $\mathrm{N}\cdot\mathrm{m}^{-\alpha}$ and an exponent $\alpha > 1$, which are functions of the elastic properties and geometries of the contacting bodies. These two parameters can be selected either from physical measurements, see *e.g.* [37], or by using ad-hoc values (as in the penalty approach employed here). In our case, the interpenetration must remain small, leading to very large values of K_c, usually in the range of 10^7 $\mathrm{N}\cdot\mathrm{m}^{-\alpha}$ to 10^{13} $\mathrm{N}\cdot\mathrm{m}^{-\alpha}$. The value of the exponent α shall be taken as 1.5 if one considers a Hertz collision between two spheres, however other choices are also admitted, see *e.g.* [35, 36, 38, 39].

One property of the contact force (7) is that it derives from a potential $\psi(x,t)$:

$$f(x,t) = \frac{\partial \psi}{\partial \eta}, \quad \text{with} \quad \psi(x,t) = \frac{K_c}{\alpha+1}\left[\eta\right]_+^{\alpha+1}. \tag{8}$$

As shown in [34–36], this property is useful to write the energy of the system and derive an energy-conserving scheme at the discrete level.

Eqs. (7) and (8) describe a collision without any dissipation of energy either due to friction or damping at the contact points. The model can be enhanced by adding a local damping term in the contact force, following Hunt and Crossley [35, 40]. However in this paper, it is assumed that contact is without dissipation.

2.4. Modal approach

A modal approach is used to solve for the dynamics of the VI-ABH in time. In this Section, the computation of the eigenproblem, which needs special care due to the important change in thickness, is first introduced. Modal damping ratios are then obtained from the complex eigenfrequencies in section 2.4.2. The modal expansion is finally derived in Section 2.4.3.

2.4.1. Real eigenmodes of the conservative ABH beam

At first the eigenmodes of the beam without losses are computed, so that Eq. (2) is considered, without the right-hand side term : $f = p = 0$. For this computation, the real part of the bending stiffness D, the modified density ρ in Eq. (5) and the thickness h in Eq. (6) are used.

In order to cope with the large variations of the thickness along the ABH edge, a finite difference method with a non-uniform grid spacing is introduced, following [9, 23, 41]. A coordinate change is introduced so as to transform the physical mesh grid into a transformed one where a modified equation of motion is solved [41]. Practically, a coordinate change is introduced that maps the physical coordinate $x \in [0, L]$ onto a uniform mesh grid $\lambda \in [0, 1]$. The one-to-one map between λ and x is selected according to the variations of the flexural wavelength and reads :

$$\lambda(x) = \frac{1}{\bar{X}}\int_0^x \frac{1}{\sqrt{h\left(\theta\right)}}\mathrm{d}\theta\,, \qquad \text{with} \qquad \bar{X} = \int_0^L \frac{1}{\sqrt{h\left(\theta\right)}}\mathrm{d}\theta\,. \tag{9}$$

The partial derivatives are then rewritten following

$$\frac{\partial u}{\partial x} = \frac{\partial u}{\partial \lambda}\frac{\partial \lambda}{\partial x} = \frac{h^{-1/2}}{\bar{X}}\frac{\partial u}{\partial \lambda}, \tag{10}$$

in order to obtain the transformed equation to be solved on the λ domain. The uniform grid spacing λ_l is then simply introduced as $\lambda_l = l\Delta_\lambda$, for $l = 1, ..., N_\lambda$, with $\Delta_\lambda = 1/N_\lambda$ the spatial step. All the functional fields appearing in the linearized Eq. (2) are computed on these grid points, with for example $D_l = D(\lambda_l)$, $\rho_l = \rho(\lambda_l)$, ... The transverse displacement is written as $u(x,t) = \varphi(x)\,\mathrm{e}^{j\omega t}$ for the eigenvalue analysis, with $\varphi(x)$ the unknown, which is discretized accordingly, with $\varphi_l = \varphi(\lambda_l)$, and ω the radian eigenfrequency. The second-order derivative appearing in Eq. (2) is approximated with the following discrete operation:

$$\frac{\partial^2 u}{\partial x^2} \approx \frac{h_l^{-1/2}}{\bar{X}^2}\delta_{\lambda+}\left(\left(\mu_{\lambda-}h_l^{-1/2}\right)\delta_{\lambda-}u_l\right), \tag{11}$$

where the discrete operators for space $\delta_{\lambda+}$ and $\delta_{\lambda-}$ and for averaging $\mu_{\lambda-}$ are given in Appendix. These discrete operators lead to a positive-definite definition of the discrete energies of the system, hence ensuring a good convergence and stability of the method [41].

Considering (11), the eigenfrequencies and eigenvectors are found by solving numerically the following equation:

$$-\rho_l A_l \omega^2 \varphi_l + \frac{h_l^{-1/2}}{\bar{X}^4}\delta_{\lambda+}\left(\left(\mu_{\lambda-}h_l^{-1/2}\right)\delta_{\lambda-}\left(D_l h_l^{-1/2}\delta_{\lambda+}\left(\left(\mu_{\lambda-}h_l^{-1/2}\right)\delta_{\lambda-}\varphi_l\right)\right)\right) = 0. \tag{12}$$

The boundary conditions are also expressed at the discrete level following the same scheme. Their complete expressions are given in Appendix. The numerical solution of Eq. (12) together with the boundary conditions give the undamped eigenmodes of the system, denoted as $\varphi_k(x)$ for the eigenmode shape and ω_k for the radian eigenfrequency, with $k = 1, ..., N_m$, where N_m is the number of modes considered.

2.4.2. Complex eigenvalues

A second computation is realized for taking losses into account. More specifically, Eq. (12) with the associated boundary conditions is solved by now considering the complex bending stiffness D^* introduced in Eq. (4). As a result of this computation, complex eigenfrequencies $\omega_k^\star$ are retrieved. The relationship between the new complex eigenfrequencies and those computed in the conservative case ω_k is known and reads

$$j\omega_k^\star = \omega_k\left(-\xi_k \pm j\sqrt{1-\xi_k^2}\right), \tag{13}$$

where ξ_k is the modal damping ratio. Hence from the computation with damping included, the real part of (13) is used in order to identify the modal damping ratios ξ_k that will serve as input to the modal equation.

2.4.3. Modal expansion

Using the standard modal expansion method, the unknown beam displacement is written as

$$u(x,t) = \sum_{k=1}^{N_m} \varphi_k(x) q_k(t), \tag{14}$$

where $q_k(t)$ is the modal coordinate associated to mode $\varphi_k(x)$, and N_m is the number of modes used for the expansion. For any two modes $\varphi_k(x)$ and $\varphi_p(x)$, the eigenshape functions are orthogonal and have been normalized with respect to the mass,

$$\int_0^L \rho\left(x\right) A\left(x\right) \varphi_k\left(x\right) \varphi_p\left(x\right) \mathrm{d}x = \delta_{kp}, \tag{15}$$

with δ_{kp} the Kronecker delta function.

Inserting (14) in the complete equations of motion (2), multiplying by another test function $\varphi_p(x)$, integrating over the size of the domain and using the orthonormality properties of the eigenmodes, one obtains :

$$\ddot{q}_k + 2\xi_k\omega_k\dot{q}_k + \omega_k^2 q_k = p_k + f_k \tag{16}$$

where $\dot{q}_k$ and $\ddot{q}_k$ are the first and second derivative of the modal amplitude with respect to time, ω_k and ξ_k represent respectively the eigenfrequency and modal damping ratio computed as explained just before, p_k and f_k stand respectively for the modal projection of the external excitation and contact force to each mode such that $p_k = \int_0^L p\left(x,t\right) \varphi_k\left(x\right) \mathrm{d}x$ and $f_k = \int_0^L f\left(x,t\right) \varphi_k\left(x\right) \mathrm{d}x$.

The last step of the numerical model consists in solving the problem in the time domain. A special attention is paid to take into account the non-smooth contact law, this is the subject of the next Section.

2.5. Time integration

The temporal scheme used for the numerical integration has been introduced in [36] for string vibrations. It is based on earlier works using other space discretizations and not referring to a modal approach [35, 38, 41]. An adaptation to the case of VI-ABH beam is here proposed. The interested reader is referred to [36] for a complete presentation of the scheme and its properties. distinctive feature of the method is to rely on a modal approach in order to treat properly the losses as individual modal loss factors that can be tuned at will. Another advantage of using the modal expansion is that an exact scheme for computing the solution when no contact is at hand can be applied. Finally, the contact force is computed in space domain, leading to an overall conservative scheme with unconditional stability.

The contact force occurs only on the set of discrete contact points, the space locations of which are known. One can take advantage of this feature in order to compute the collision term only at these points. It will result in important gain savings in computation [42]. Let us introduce $\mathbf{X} = [x_F,\ x_{c1},\ x_{c2}, \ldots,\ x_{cN_c}]$ the vector consisting of all the discrete contact points x_{ci} plus the point location of the excitation force x_F. Let $\mathbf{u}^n = u\left(\mathbf{X}, n\Delta t\right)$ be an approximation of the transverse displacement selected at position $\mathbf{X}$ for time $t_n = n\Delta t$. The relationship with the modal expansion (14) allows one to write $\mathbf{u^n} = \mathbf{S}\mathbf{q^n}$, where $\mathbf{q}^n = \left[q_1\left(n\Delta t\right), ..., q_{N_m}\left(n\Delta t\right)\right]^T$ the vector of modal amplitudes and $\mathbf{S}$ is a rectangular matrix with entries $S_{ij} = \varphi_j\left(X_i\right), \forall\left(i,j\right) \in \{1, ..., N_c+1\} \times \{1, ..., N_m\}$.

The update for the displacement vector $\mathbf{u}^{n+1}$ is directly computed from previous modal displacements $\mathbf{q}^n$, $\mathbf{q}^{n-1}$. Using $\mathbf{u^{n+1}} = \mathbf{Sq^{n+1}}$, we have :

$$\mathbf{u}^{n+1} = \mathbf{SCq}^n - \mathbf{S\tilde{C}q}^{n-1} + \Delta t^2 \mathbf{SS}^T \left(\mathbf{p}^n + \mathbf{f}^n\right). \tag{17}$$

In this update equation, $\mathbf{p^n}$ and $\mathbf{f^n}$ are respectively the vectors of external and contact forces computed at time n. $\mathbf{C}$ and $\tilde{\mathbf{C}}$ are two diagonal matrices with entries :

$$C_{kk} = e^{-\omega_k \xi_k \Delta t}\left(e^{\omega_k \sqrt{\xi_k^2-1}\Delta t} + e^{-\omega_k \sqrt{\xi_k^2-1}\Delta t}\right), \quad \tilde{C}_{kk}{=}e^{-2\omega_k \xi_k \Delta t}. \tag{18}$$

Note that this particular choice is related to the exact scheme for the free flight phases of the vibration where no contact is involved [36, 41]. Finally the contact force $\mathbf{f^n}$ is computed via

$$\mathbf{f^n} = \frac{\psi(\boldsymbol{\eta}^{n+1}) - \psi(\boldsymbol{\eta}^{n-1})}{\boldsymbol{\eta}^{n+1} - \boldsymbol{\eta}^{n-1}}, \tag{19}$$

this choice being related to the derivation of a conservative scheme, as shown in [35, 36]. Note finally that the scheme is of order two and implicit; a Newton-Raphson procedure is needed to compute the update because of the nonlinear character of the regularized restoring force describing the contact.

3. Numerical Results

In this Section, a typical ABH beam is selected and analysed firstly without collision. The convergence of the numerical method with respect to discretization parameters is outlined. Then the effect of the vibro-impact to enhance the damping efficiency is investigated.

3.1. Modal parameters and mobilities of a typical ABH beam

A typical ABH beam is considered: it is made of aluminum and its profile is given by Eq. (6). All geometrical and material parameters are listed in Table 1. The overall resulting design is close to the one of experimental beam demonstrators of previous works [9]. Note that the uniform beam with constant thickness defined in the first line of Table 1 will be used as a reference case. From this design and following [22], the cut-on frequency of the ABH effect is found to be $f_c = 374$ Hz, which corresponds well to Fig. 2 in which the first peaks above f_c start to be attenuated, the other ones above 500 Hz being pretty much damped.

The solutions of the eigenvalue problem are computed with a non-uniform grid such that $N_\lambda = 2000$. Fig. 2 shows that as expected, the modal damping ratios of the uniform reference beam (blue circles) are constant with frequency while those of the ABH beam (red stars) are approximately 10 times larger above the cut-on frequency due to the ABH effect, which leads to a typical increase in amplitudes and shrinkage of wavelengths of the modal shapes in the tapered area. Fig. 3 shows 6 eigenmode shapes computed. One can observe that for the higher modes (*e.g.* modes 15 and 30 shown in Fig. 3(e-f)), the vibration amplitude is especially important in the ABH region. On the other hand, ξ_k remains small for the first four modes due to the weak efficiency of the ABH effect at low frequency, which results only

Beam parameters					
L(m)	h_0(mm)	b(mm)	E_b(pa)	$\rho_b(kg \cdot m^3)$	$\eta_b(\%)$
0.8	4	20	70G	2700	0.2
ABH termination parameters					
x_{abh}(m)	x_{end}(m)	$h_t(\mu$m)			
0.71	0.80685	20			
Visco-elastic layer at $[x_{abh}, L]$					
$h_l(\mu$m)	E_l(Pa)	$\rho_l(kg \cdot m^3)$	$\eta_l(\%)$		
400	10M	1000	160		

Tab. 1: Geometrical and material parameters selected for the studied ABH beam.

in a slight modification of the modal shapes. These results are fully in line with simulations of previous works [9]. Note that three contact points locations are also included in Fig. 3(a-b), this will be discussed later.

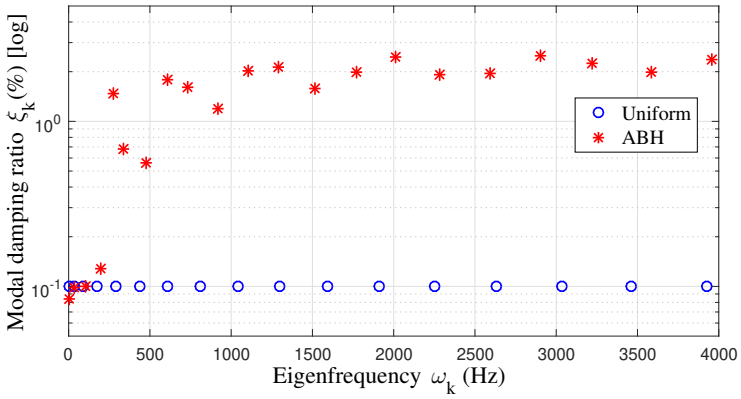

Fig. 2. Modal damping ratio ξ_k versus eigenfrequency ω_k for the uniform beam (blue circles) and ABH beam (red stars), following parameters given in Table 1.

The response to a $[0, 5000]$ Hz white noise excitation applied in x_F is then simulated. The simulation is 4s long with sampling frequency $F_s = 6 \times 44100$ Hz. A Fourier transform is applied to both the velocity and driving force that are recorded at x_F. Fig. 4 shows the input mobility defined as the ratio between the velocity and the input force spectra at x_F. As expected, the excellent damping properties of the ABH above the cut-on frequency leads to strongly attenuate the resonance peaks of more than 20dB, while the first low frequencies resonances remain sharp with large amplitude. The goal of the next Sections is to study the possible enhancement of low-frequency efficiency of the ABH effect when combined with an added vibro-impact.

3.2. Convergence study

This section aims at correctly setting the numerical parameters in order to obtain converged results in the next sections.

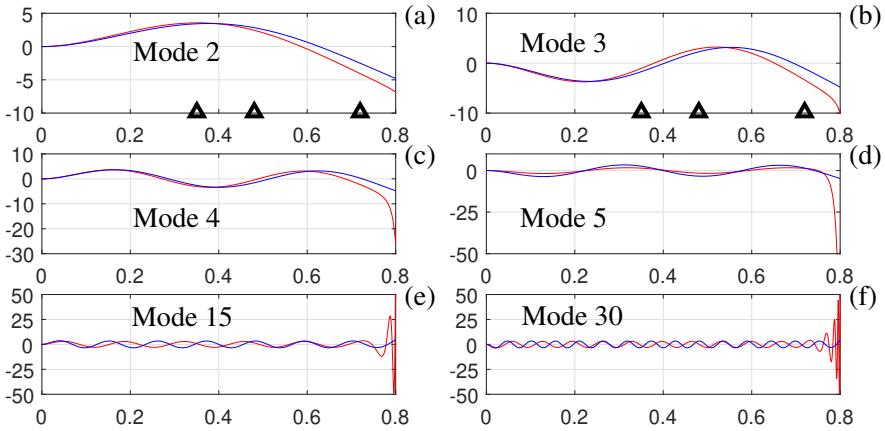

Fig. 3. Comparison of a few mode shapes between the uniform beam (blue line) and the ABH beam (red line), following parameters given in Table 1. Also included in panels (a)-(b): location of three contact points, at x_c=35 cm, 48 cm and 72 cm.

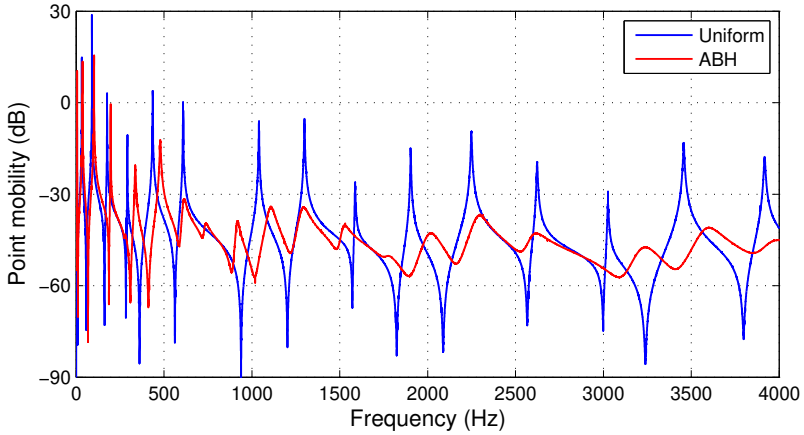

Fig. 4. Point mobility of the uniform beam (blue line), compared to that of an ABH beam (red line). Beam parameters are given in Table 1. Excitation and measurement points are both located at $x_F = 24$ cm, with a large band white noise excitation on $[0, 5000]$ Hz, with amplitude 1 N. Simulation parameters are: grid number N_λ=2000, $F_s = 6 \times 44100$ Hz and truncated mode number N_m=50.

First, the number of grid points, only used to calculate the eigenmodes, is set to $N_\lambda = 2000$. The first 100 modes are converged with a maximal error of 0.2% on the modal frequencies ω_k and 5% on the modal damping factors ξ_k, when compared to a reference case calculated with $N_\lambda = 3000$. The computing time for this operation is negligible as the result is obtained immediately on a standard computer. Consequently, $N_\lambda = 2000$ is selected for all following simulations.

Concerning the number of modes N_m, one has to ensure that N_m is large enough so as to represent properly the small wavelength dynamics produced by the contacts. As shown in Table 2, the eigenfrequency of mode 75 is at 51.1kHz and mode 100 at 90.9kHz. As the

computational time for simulations with 100 modes is not too important, $N_m = 100$ has been selected for all the simulations, ensuring for a correct representation.

Mode n	1	2	3	4	5	6	7
f_n(Hz)	5.9	36.7	101.4	196.2	278.5	336.5	478.9
Mode n	8	9	10	25	50	75	100
f_n(Hz)	611.4	732.3	916.0	5.6k	22.6k	51.1k	90.9k

Tab. 2: Eigenfrequencies of the ABH beam

The most difficult parameter to select is the sampling frequency F_s. The contact dynamics brings about strong nonlinearities and the numerical problems for contact dynamics are known to be stiff, so that very large F_s values are generally used for accurate simulations of vibro-impact problems [43]. In order to properly select F_s, a detailed convergence study is then conducted.

The case study is that of the ABH beam with parameters given in Table 1, excited with a band-limited white noise in the range $[0, 1000]$ Hz, the excitation point being located in the uniform region of the beam, at $x_F = 24$ cm. The amplitude of the band-limited noise excitation is set to 1 N. As the impact dynamics is critical for determining the correct sampling frequency F_s to be retained, two cases with respectively one and three contact points are selected, with a gap h_c equal to zero in each case, which means that the contact points are flush with the lower part of the beam. The single contact point is located at x_{c1} = 72 cm, *i.e.* one centimeter after the beginning of the wedge profile. The three contact points are located at $x_{c1} = 70$ cm, $x_{c2} = 72$ cm and $x_{c3} = 74$ cm. These two cases have been selected as giving a representative dynamics allowing one to select properly a correct sampling frequency F_s.

To evaluate the convergence, the L^2 relative error between a given tested vector V_c and a reference vector V_{ref} is defined as

$$R = \frac{\|V_{ref} - V_c\|}{\|V_{ref}\|}, \tag{20}$$

with $\|\cdot\|$ the L^2 norm.

First, the convergence of time signals is shown in Fig. 5(a). The simulated signals are 0.5 s long, involving around 50 impacts, which is considered as sufficiently large to represent correctly the full dynamics of the system. The vectors in (20) are thus taken as the output displacements along these 0.5 s, either at the excitation point x_F, or at the contact point x_{c1}. The behaviour of the convergence curves shown in Fig. 5(a) is in the line of previous studies, see *e.g.* [36]. One can observe that the convergence is almost independent from the ouput point, meaning that the rich spectral content generated by the contact is spatially distributed uniformly along the beam. The tested sampling frequencies F_s range from 10 kHz to $2^{11} \times 10$ kHz, *i.e.* approximately 20 MHz, so that V_{ref} . For a single contact, a plateau followed by a linear convergence with a slope around 2 (the order of the scheme) is observed

and leads to a residual error of about 10^{-3} with $F_s = 2^{10} \times 10$ kHz=10.24 MHz. For three contacts layout, the convergence is harder to achieve and an error of about 7×10^{-2} is obtained with $F_s = 10.24$ MHz.

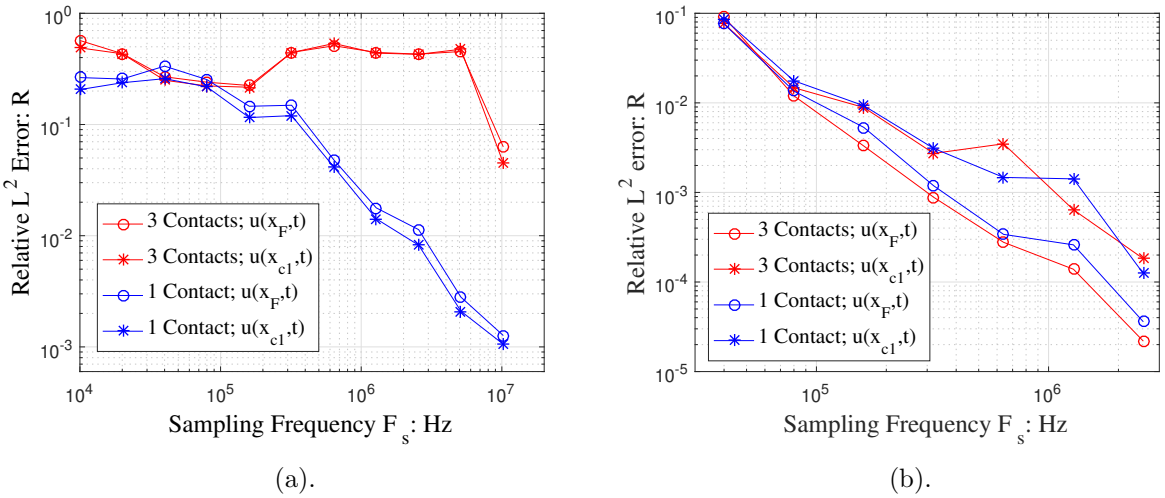

(a). (b).

Fig. 5. Convergence study as function of the sampling frequency F_s. Relative L^2 error following Eq. (20) on (a) the time signal, (b) the frequency spectrum. Different cases are : 1 contact point located at $x_{c1} = 72$ cm, ouput measurement as the displacement at either the excitation point x_F (blue circle) or the contact point x_{c1} (blue star); 3 contact points located at $x_c = [70, 72, 74]$ cm, ouput measurement as the displacement at the excitation point (red circle) or the first contact point (red star). Stiff contact with $\alpha = 1.5$, $K_c = 10^{11}$ N$\cdot$m$^{-1.5}$, and no gap between the and the beam : h_c=0. Temporal convergence with signals computed in the first 0.5 seconds of simulation for the beam excited with a $[0, 1000]$ Hz band limited noise. Spectral convergence with spectrum computed from 3 seconds of simulations and up to 20 kHz.

As already noticed by several investigations on contact dynamics [36, 43, 44], the convergence of time signals is especially difficult to achieve rigorously, due to inevitable residual phase shifts. Consequently the error on time signals may not be the best indicator to ensure convergence. Furthermore, the key point of this work is to study the energy transfer from low to high frequencies, due to contact dynamics. Hence, the convergence of Fourier spectrum may be more representative of the accuracy of the simulated results. From this, the convergence study now focuses on the Fourier spectrum: the vectors V_c, V_{ref} in Eq. (20) corresponds to the Fourier spectrum of 3.3s time signals, estimated over the frequency range [0-20] kHz. This means that the following convergence study only concerns the audible range, ultrasonic frequencies being of no interest here. Fig. 5(b) shows the results obtained with the reference case simulated with $F_s = 2^9 \times 10$ kHz=5.12 MHz. A decrease of the error is clearly observed, showing a uniform convergence with a slope near the order of the scheme. With the last sampling frequency tested $F_s = 2.56$ MHz, the error is close to 10^{-4}, which means that the frequency content up to 20 kHz is very accurately simulated.

In conclusion of this convergence study, all forthcoming simulations are done with $N_\lambda = 2000$, $N_m = 100$ and $F_s = 2.56$ MHz.

3.3. Vibro-impacts with a single contact

3.3.1. Description

To reveal the effect of the contact nonlinearity and the potential improvement it can bring to the low-frequency ABH performance, the dynamical behaviour of a VI-ABH with a single contact point is first analysed. For this first investigation, the contact point is located at $x_{c1} = 35$cm, *i.e.* in the region of constant thickness, far from the ABH wedge profile (see Fig. 3(a-b)). Note that at present this location is selected arbitrarily, the search for a location giving the best gains in efficacy will be investigated after. The constants of the contact force have been selected as $\alpha = 1.5$ and $K_c = 10^{11}$ N $\cdot$ m$^{-1.5}$, corresponding to a stiff contact between the two bodies. Four different configurations are compared in order to assess the different physical effects: case 1 corresponds to the reference beam with uniform thickness (first row of Table 1), case 2 to the ABH beam (second and third rows of Table 1), case 3 is the uniform beam with the single contact point as defined, and finally case 4 corresponds to the VI-ABH.

3.3.2. Response to a broadband excitation ([0, 5000] Hz)

Fig. 6 shows the response of the beam to a wide-band white noise excitation in the range [0, 5000] Hz, and an amplitude of 1 N. The location of the external force on the beam is at $x_F = 0.3L = 24$cm, and this value will remain the same in all subsequent simulations shown in the article. Fig. 6 shows the spectrum of the velocity response $V(\omega)$ divided by the spectrum of the excitation force $F(\omega)$, both at the excitation point. This quantity corresponds to the driving mobility for a classical linear system, even though this quantity has a well-defined sense in the linear case , it is used in this first illustration in order to see the effect brought by the nonlinearity as compared to the usual linear case without contact. The Fourier spectra are computed from a simulation lasting 5 seconds.

The two curves corresponding to cases 1 and 2 are the same as those already reported in Fig. 4. The effect of the contact nonlinearity is to bring about a very rich, high-frequency content to the response's spectrum as displayed by cases 3 and 4. This is a very important modification in the dynamics of the ABH and the question is to quantify if this drastic change brings about an improvement to the damping capacity of the device. In Fig. 6(a), one can clearly see the effect of the ABH termination by comparing cases 3 and 4: the generation of the high-frequency content is much more damped in case 4, showing that the key mechanism consisting of transferring the low-frequency content to high frequencies by the nonlinearity, where the damping properties are much more efficient due to ABH effect, is at hand. The effect may be better appreciated by looking at the zoom on the low-frequency part shown in Fig. 6(b). One can see that the contact nonlinearity replaces a smooth Fourier content with sharp resonances to a blurred and nonsmooth spectrum, which is generally lower in amplitude, especially in the vicinity of the eigenfrequencies. This means that the contact nonlinearity somehow breaks the sharp resonances where most of the energy is concentrated, in favour of a broadband Fourier spectrum with smaller amplitudes.

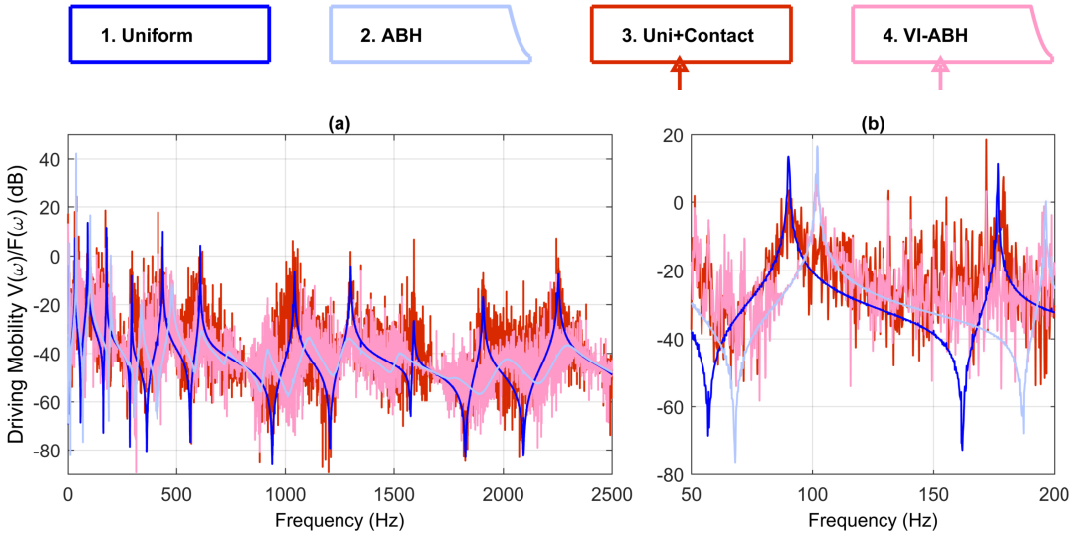

Fig. 6. (a) Driving mobility for the uniform (reference) beam, case 1; the ABH beam, case 2; the uniform beam plus single contact, case 3; and the VI-ABH with single contact, case 4. Beams excited with a [0, 5000] Hz band limited noise, spectra calculated from the response at exciting point during time interval [1 5]s. (b) Zoom in the low frequency part. α=1.5, $K_c = 10^{11}$ N $\cdot$ m$^{-1.5}$, no gap h_c=0.

3.3.3. Response to a band-limited excitation ([0, 500] Hz)

In order to quantify more precisely the improvement in the low-frequency part, the same simulation is now realised with a white noise excitation with a band limited to [0, 500] Hz. Fig. 7 shows the velocity spectrum of the response at the excitation point for the same four cases. Note that from now on, only the spectrum of the output velocity is considered in order to quantify the different dynamical behaviours.

Fig. 7(a) shows that for the reference and ABH beam, case 1 or 2, the behaviour is linear; energy is only present in the excitation band as expected. As the contact is present, cases 3 and 4, a strong nonlinearity is at hand resulting in a rapid and efficient transfer to high frequencies. Comparing case 3 and 4, once again the ABH effect is clearly visible with a more important decrease in the amplitudes of the high frequency part, showing that the two effects searched for an improvement are playing their roles. The energy transfer allows to reduce the vibrational amplitudes in the low-frequency part of the spectrum, before 500 Hz, as confirmed by the zooms presented in Figs. 7(b,c,d). The effect underlined in Fig. 6 is evidenced again, as the sharp resonance peaks obtained with linear cases 1 and 2 are replaced by a bumpy, irregular spectrum without outstanding peaks. The decrease of the resonance peaks is particularly impressive around 35 Hz, see Fig. 7(c), *i.e.* in the vicinity of the second eigenfrequency, showing that the desired effect works perfectly well there. This fact can be explained by the location of the contact point for this study, at $x_{c1} = 35$ cm, corresponding to a local maximum of mode 2 (see Fig. 3(a)). On the other hand, this location is close to a node of mode 3 (see Fig. 3(b)), and one can observe in Fig. 7(d) that the effect is not so important in the band [85, 105] Hz. This point will be further discussed when considering

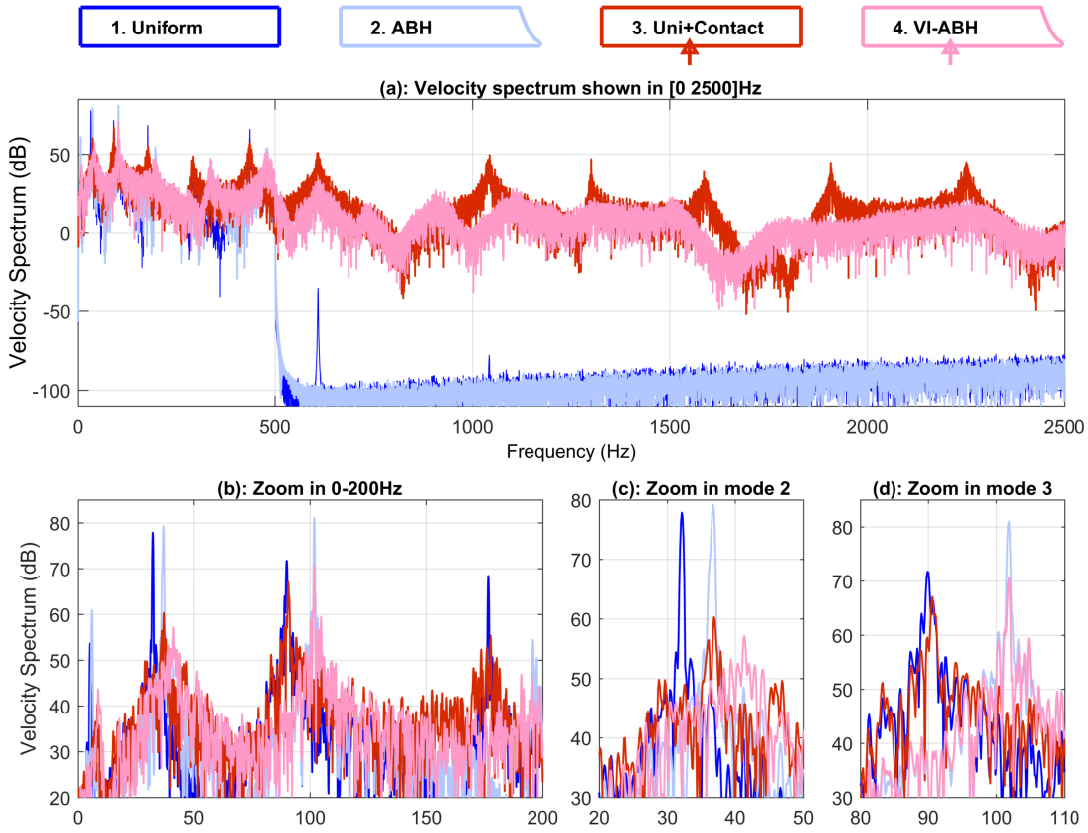

Fig. 7. Velocity spectrum for a low frequency [0, 500] Hz band-limited noise excitation, amplitude 1 N. Comparisons between four different cases, spectra computed from 4 seconds steady state time simulation. (a) global view on the band [0, 2500] Hz, (b,c,d) : zooms on different parts of the spectra.

variations of the position of the contact point in order to find a better location.

3.3.4. Efficiency of the energy transfer

In order to offer a more quantitative view of the improvement brought by the nonlinearity, an indicator is introduced that compares the power spectrum in different frequency bands. More precisely, the indicator I is defined as

$$I = 10\log_{10}\left(\frac{\int_{f_0}^{f_{end}} a_c^2 \,\mathrm{d}f}{\int_{f_0}^{f_{end}} a_{ref}^2 \,\mathrm{d}f}\right), \tag{21}$$

where a denotes the power spectrum of velocity at excitation point, the subscript c or ref referring respectively to the current case and the reference case (*i.e.* the uniform beam corresponding to case 1). This energy performance indicator is used to assess the gains obtained in vibration reduction in the range $[f_0, f_{end}]$. More precisely, three indicators are introduced. The first one is $I_{[0,\, f_e]}$, where $f_e = 500$ Hz corresponds to the cut-on frequency

found in Fig. 4. The two other indicators are $I_{[f_e,\,5f_e]}$, which is concerned with the high-frequency part of the spectrum; and $I_{[0,\,5f_e]}$ which quantifies the overall performance.

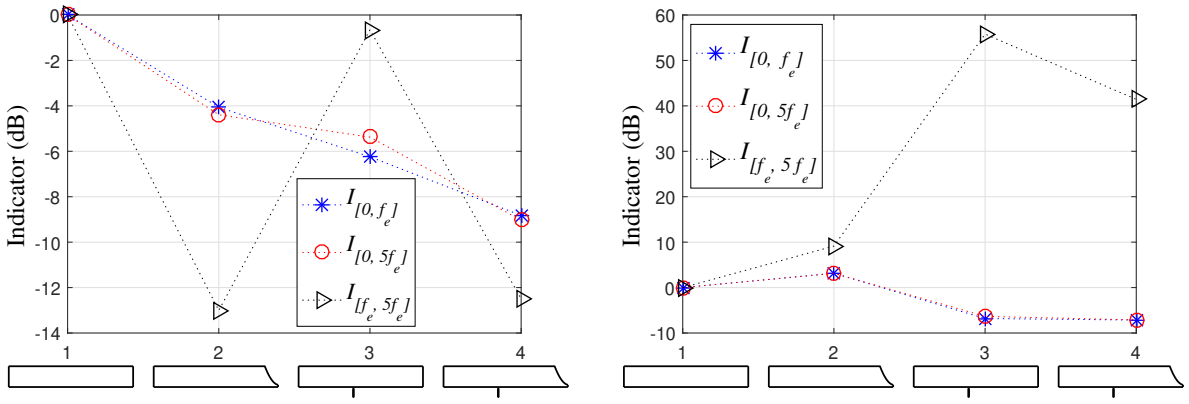

(a). (b).

Fig. 8. Indicators $I_{[0,\,5f_e]}$, $I_{[0,\,f_e]}$ and $I_{[f_e,\,5f_e]}$ calculated from the responses to (a) full band noise excitation [0, 5000] Hz, (b) low frequency noise excitation restricted to the band [0, 500] Hz, amplitude 1 N. Case 1: uniform beam. Case 2 : ABH beam. Case 3 : uniform beam and a single contact point at $x_{c1} = 35$cm. Case 4 : VI-ABH with single contact at $x_{c1} = 35$cm. α=1.5, $K_c = 10^{11}$ N $\cdot$ m$^{-1.5}$, no gap h_c=0.

Fig. 8 shows the different values of the three indicators, for the two cases shown in Fig. 6 and Fig. 7, where the reference used for the comparisons (a_{ref} in Eq. (21) is case 1, the uniform beam. The consequence of this choice is that in Fig. 8, the value of case 1 is always zero. Negative values of the indicator give a quantitative idea of the gain brought by the different configurations tested. Fig. 8(a) refers to the white noise excitation on the band [0, 5000] Hz. The main observation is that the two curves for $I_{[0,\,5f_e]}$ and $I_{[0,\,f_e]}$ are very close, meaning that most of the energy is effectively concentrated in the low frequency domain of the spectrum, *i.e.* in the band [0, 500] Hz where the most proeminent peaks are found. Comparing case by case, one can see that the ABH effect offers a global decay of energy down to -4 dB. A very important reduction is obtained in the high-frequency range, as attested by the behaviour of $I_{[f_e,\,5f_e]}$ which goes rapidly down to -13 dB. Case 3, the uniform beam with a single contact point, is very interesting as it shows that a global decay of $I_{[0,\,5f_e]}$ down to -5 dB can be obtained only thanks to the contact nonlinearity, and without considering any black hole effect. Here the energy transfer due to the non-smooth nonlinear characteristic already gives good results with a very important decrease of energy in the low frequency range ($I_{[0,\,f_e]}$ is a bit lower than -6 dB). This means that the contact nonlinearity can already be considered as an effective vibration damper since a large amount of energy is transferred rapidly to high frequencies where the losses are naturally more important. On the other hand, $I_{[f_e,\,5f_e]}$ observes a very small decrease, but since less absolute energy is present in the high-frequency part of the spectrum, the global gain is very important. Considering the VI-ABH, case 4, shows that the combination of both nonlinear and damping effect is impressive and results in a global energy decay around -9 dB, with a strong gain in low and high frequency ranges.

Fig. 8(b) shows the indicators' behaviour when excited with noise excitation the band [0, 500] Hz. Once again $I_{[0,\,5f_e]}$ and $I_{[0,\,f_e]}$ have almost the same values, which means that most of the energy is concentrated in the excitation band. On the other hand $I_{[f_e,\,5f_e]}$ appears to rise to very large values, but one must keep in mind that this is relative to very small absolute values of the energy in the high-frequency band, consequently these important values does not reflect an incorrect performance of the cases tested, the most important information being the observed decrease for $I_{[0,\,5f_e]}$ for case 3 and 4. Case 2, the ABH beam, shows an increase as compared to case 1, underlining once again the underwhelming behaviour of the ABH in the low frequency part, under the cut-on frequency. Comparing with case 3, the uniform beam with single contact point shows an improvement with a decrease of $I_{[0,\,5f_e]}$ down to -6.3 dB. Of course, as also attested in Fig. 7, this is at the expense of the generation of a high-frequency part and a strong increase of $I_{[f_e,\,5f_e]}$. This increase can be counterbalanced by adding the black hole effect, in order to obtain both a global decrease, with $I_{[0,\,5f_e]}$ down to -7.2 dB for case 4, and a smaller increase of $I_{[f_e,\,5f_e]}$. Optimizing the damping properties of the visco-elastic layer or decreasing the thickness at the ABH truncation may increase the high-frequency damping and could be used to achieve a better picture to the vibration mitigation.

3.3.5. Influence of contact point location and gap

To conclude this section, the location of the single contact point is now varied in order to find the location of the contact points that give the best efficacy. To complete the analysis, the gap h_c is also varied in order to understand its effect. Fig. 9 illustrates the variation of indicators $I_{[0,\,f_e]}$ and $I_{[f_e,\,5f_e]}$ when modifying the location of the contact points on the abscissa: 8 different locations are tested, the positions of which are given as inset in the figure. For each case, three different values of the gap are tested: $h_c = 0$ (no gap), $h_c = 0.2$ and 0.5 mm. It is emphasized that from hereafter, we will focus on the improvement one can bring to the ABH beam, consequently the reference case used in the calculation of indicators, Eq. (21), is selected as the ABH beam without contact. Also, the excitation is always band-limited to the low frequency range [0, 500] Hz.

The effect of the gap h_c is generally to decrease the efficiency of the contact ABH beam, as it could have been expected. Indeed, the behaviour of $I_{[0,\,f_e]}$ clearly evidenced that the best results are obtained with $h_c = 0$, and increasing h_c decreases the performance, as the contact nonlinearity is less excited in the presence of a gap. Recalling that the values of $I_{[0,\,f_e]}$ and $I_{[0,\,5f_e]}$ (not shown in the figure), are almost the same, the behaviour of $I_{[0,\,f_e]}$ depending on the 8 cases tested shows that the device can be remarkable at some positions (1, 3, 6 and 8), but unsatisfactory at other positions such as 4 or 5. The best point is case 3 with the optimal performance corresponding to a physical location on the beam where both modes 2 and 3, which are the most important in the vibrational energy present below the cut-on frequency, have a local maximum (see Fig. 3(a-b), with contact point corresponding to case 3 at $x_c = 48$ cm). Consequently their sharp resonance peaks are broken down by the contact nonlinearity resulting in an important global gain in performance. The results for the other locations can also be interpreted in the light of the position of nodes and maxima

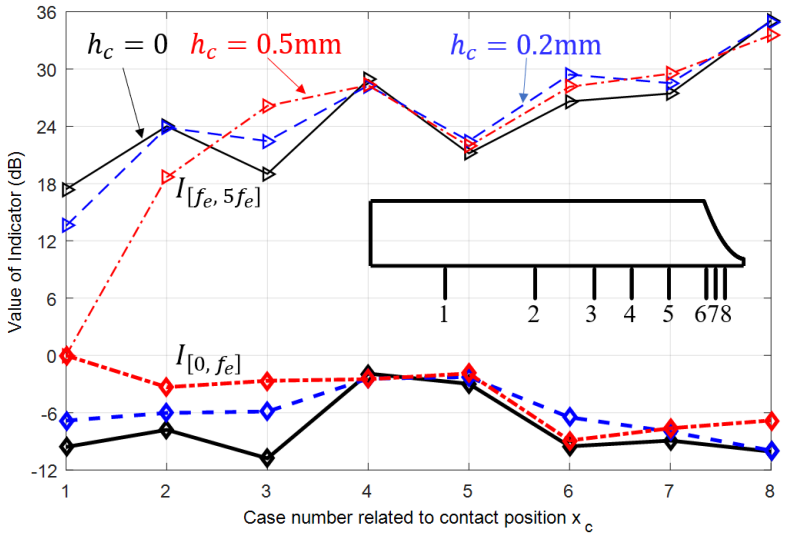

Fig. 9. Indicators $I_{[0,\,f_e]}$ and $I_{[f_e,\,5f_e]}$ as a function of the contact location x_{c1} for single contact case, and for three different values of the gap, h_c=0, h_c=0.2 mm and h_c=0.5 mm. The exact location of the contact points for cases 1 to 8 are respectively: 16 cm, 35 cm, 48 cm, 56 cm, 64 cm, 72 cm, 74 cm, and 76 cm. Excitation amplitude $A = 1$ N, Contact coefficients α=1.5, $K_c = 10^7$ N $\cdot$ m$^{-1.5}$.

of eigenmodes, showing that the knowledge of the low-frequency eigenmode shapes is crucial in order to offer an optimal control of the energy transfer in the low-frequency part of the spectrum.

3.4. Vibro-impacts with multiple contact points

Based on the interest shown above of associating vibro-impacts with the black hole effect, the goal is now to investigate if the damping mitigation can be enhanced by considering a set of contact points, instead of a single one. In parallel, the contact stiffness K_c and the excitation amplitude A will also be varied in order to understand the effects of all parameters so as to provide an optimized solution for the location of contact points. Following previous conclusions, the contact points are located at the local maxima of the first modal shapes: the first contact point is at x_{c1}= 35 cm, corresponding to the maximum of eigenmode shape 2, x_{c2}= 52 cm, corresponding to the maximum of eigenmode shape 3, and so on till 7 contact points.

Tab. 3: Interpenetrations .

K_c(N $\cdot$ m$^{-1.5}$)	10^7	10^9	10^{11}
Mean Value (mm)	1.75×10^{-2}	1.09×10^{-3}	4.97×10^{-5}
Maximum Value (mm)	6.38×10^{-2}	5.55×10^{-3}	5.91×10^{-4}

Fig. 10 shows the evolution of the indicators $I_{[0,\,f_e]}$ and $I_{[f_e,\,5f_e]}$ when increasing the number of contact points, for three values of the contact stiffness K_c. It reveals that the

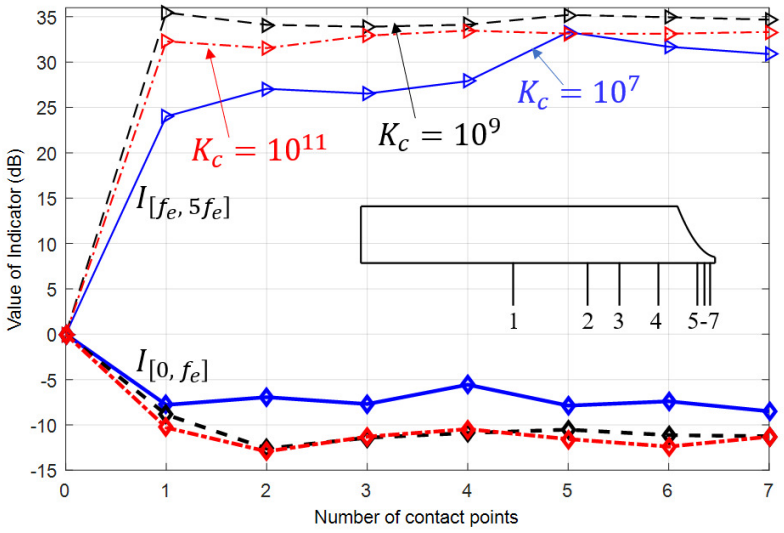

Fig. 10. Variations of $I_{[0,\, f_e]}$ and $I_{[f_e,\, 5f_e]}$ as the number of contact points increases, compared among three different values of contact stiffness, $K_c = 10^7$ N $\cdot$ m$^{-1.5}$ (blue solid lines), $K_c = 10^9$ N $\cdot$ m$^{-1.5}$ (black dashed lines) and $K_c = 10^{11}$ N $\cdot$ m$^{-1.5}$ (red dash-dotted lines). The exact location of the contact points for cases 1 to 7 are chosen as the local vibration maxima of the eigenmodes 2 to 8. Excitation amplitude $A = 1$ N, no gap $h_c = 0$, α=1.5.

larger is K_c, the better are the mitigation performances. This is clearly related to the fact that the stiffer the contact is, the more high frequencies are created at each contact and thus the energy transfer is improved. In order to give physical insight to the values of K_c used in the simulations, the mean and maximal values of the interpenetrations are given in Table 3, revealing that $K_c = 10^{11}$ N$\cdot$m$^{-1.5}$ is very stiff with a mean interpenetration between the two contacting bodies on the order of 10^{-5} mm, whereas when $K_c = 10^7$ N $\cdot$ m$^{-1.5}$, the interpenetration is not negligible anymore, around 10^{-2} mm.

Second, only very few contact points are needed to improve the mitigation performance at low frequencies. In the simulated examples, $I_{[0,\, f_e]}$ shows a significant decrease when adding a second contact point but seems to be ceiled or even downgraded for more added contact points. This can be related to the fact that a very small number of modes (only 4 under the cut-on frequency) are concerned. The conclusions may be changed for other holding structures and ABH designs where more modes are in the low-frequency range. Other types of arrangements for the of contact points could also be tested, and, as it will be shown after, in some cases more than two contact points may be more optimal.

3.5. Other rules for contact points location

For that purpose, three different ideas are numerically tested. The first arrangement considers that the interdistance between contact points has to match the wavelength corresponding to the first modes of the beam. More precisely, interdistance corresponding to 1/8 of the wavelengths are considered so as to fit with the length of the beam. Note also that

as the wavelength depends on the thickness, the interdistance is computed by taking wedge variations into account. This choice results to configuration 1 shown as inset in Fig. 11, where the distance between the first two points is 1/8 the wavelength of mode 1, and so on. Two other configurations with a constant interdistance, thus creating a Dirac Comb, are also tested, leading to configurations 2 and 3 shown as inset in Fig. 11. For configuration 2, a fixed interdistance of 2 cm from $x_{c1} = 64$cm to $x_{c8} = 78$cm is selected. For configuration 3, the first four points are placed in the uniform area from $x_{c1} = 40$cm to $x_{c4} = 70$cm with a fixed interdistance of 10 cm, then the latter four contact points are in the acoustic black hole area, from $x_{c5} = 72$cm to $x_{c8} = 78$cm, with a smaller interdistance of 2 cm.

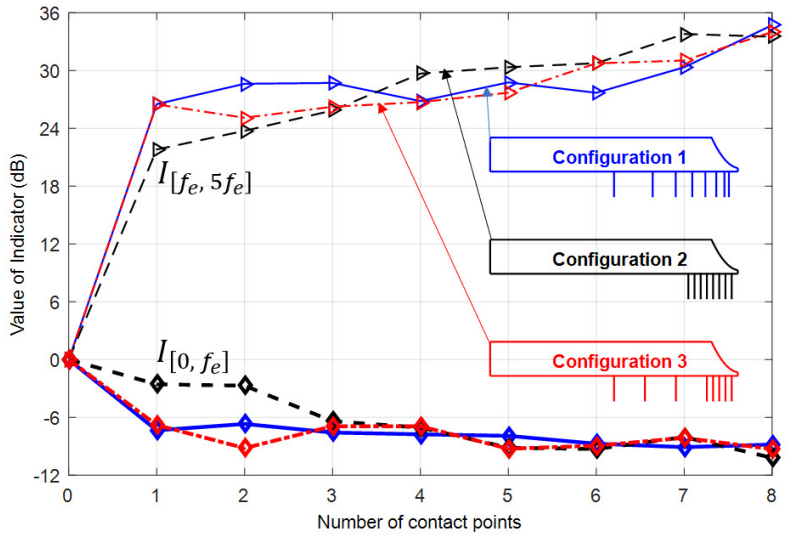

Fig. 11. Variations of $I_{[0,\, f_e]}$ and $I_{[f_e,\, 5f_e]}$ as number of contact points increases, compared among three different configurations of contact points. Configuration 1: interdistance determined by the wavelength corresponding to the first modes of the beam, the distance between the first two points is 1/8 the wavelength of mode 1, and so on. Configuration 2, Dirac Comb with fixed interdistance of 2 cm from $x_{c1} = 64$cm to $x_{c8} = 78$cm. Configuration 3, the first four points placed in the uniform area from $x_{c1} = 40$cm to $x_{c4} = 70$cm with interdistance of 10 cm, the latter four points posed in the acoustic black hole area, from $x_{c5} = 72$cm to $x_{c8} = 78$cm, with a smaller interdistance of 2 cm. α=1.5, $K_c = 10^7$ N $\cdot$ m$^{-1.5}$, $A = 1$ N, $h_c = 0$.

Fig. 11 shows the behaviour of $I_{[0,\, f_e]}$ and $I_{[f_e,\, 5f_e]}$ for these three configurations, by also selecting an increasing number of points, and for $K_c = 10^7$ N $\cdot$ m$^{-1.5}$. One can observe that for a small number of points, the deviations between the three layouts are important, the second one being the less effective. But from 3-4 points, the values of $I_{[0,\, f_e]}$ are very close so that the dependence on the configuration becomes less important. Note also that the effect of increasing the number of contact points is more important than for the cases simulated in Fig. 10, however the indicator values obtained at convergence are roughly the same, showing that from a number of contact points an optimal damping capacity is obtained which does not depend too much on their locations.

3.6. Transient dynamics

We now turn to the case where the beam is excited by an impact in order to assess the damping capacity in a transient regime instead of a permanent regime as studied in the previous sections. This will allow for a different view of the improvement that can be awaited from the device, by observing the decays in the temporal regime. The ABH beam is thus now excited by a raised cosine at the same excitation point x_F where the harmonic force was located. The external excitation $p(x,t)$ in Eq. (2) now reads $p(x,t) = r(t)\delta(x - x_F)$ with δ the Dirac delta function and $r(t)$ the temporal content which reads:

$$r(t) = \begin{cases} \frac{A}{2}\left[1 + \cos\left(\pi(t - t_0)/T_w\right)\right] & \text{if} \quad |t - t_0| \leq T_w; \\ 0 & \text{if} \quad |t - t_0| > T_w. \end{cases} \tag{22}$$

Fig. 12(a) shows an example of the temporal content, where the amplitude A in N has been set to 1, t_0 refers to the time where the impulse force is maximum and equal to A ($t_0 = 50$ ms in the figure). T_w is half of the time where the input force is non-zero ($T_w = 2$ ms in the figure). The spectral content of this input force is similar to a sine cardinale, and the maximum of the input energy is located between 0 and the first minimum at $1/T_w$. In order to be in the line of the previous investigations, $T_w = 2$ ms in all subsequent simulations, so that the energy sent to the beam is concentrated below 500 Hz.

Fig. 12(b) shows the displacement of the beam after the impact, measured at point $x = x_F = 0.3L$, and compares the case of the uniform beam with the VI-ABH having 7 contact points. For this computation, the seven contact points are located following the rule of using the maximal values of the first eigenmodes (see configuration 1 in Fig. 11), and the stiffness of the contact is selected as $K_c = 10^7$ N $\cdot$ m$^{-1.5}$, in order to see the effect in the less optimal case. In this case of transient vibrations, the effect of the impacts to damp out the vibrations is impressive. Whereas the vibration of the uniform beam takes around 10 seconds to be damped out, being completely driven by the very small values of modal damping ratio of the modes present in the excited frequency band, the energy transfer due to the contact nonlinearity spreads out this energy, leading to a very fast decay of the vibration, which is damped out in less than 2 seconds.

Fig. 12(c) compares four cases, where the envelope of the displacement signals have been extracted for better readability. The envelope is computed using the Hilbert transform. The four cases compared are the same as in Section 3.3 : the uniform beam, the ABH beam without contact, the uniform beam with contact and the VI-ABH. In the last two cases, seven contact points are used following the rule of the maximum of the first eigenmode shapes. Fig. 12(c) shows undoubtedly that when the frequency content of the excitation is below the cut-on frequency, the ABH beam brings only a little improvement as compared to the uniform beam. This, once again, underlines the poor damping capacity of the ABH in the low-frequency range. On the other hand, one can observe that for transient responses, the uniform beam with contacts shows a better mitigation capacity, only by transferring energy to higher modes. Adding the ABH effect shows that the faster decay of energy is obtained with the VI-ABH.

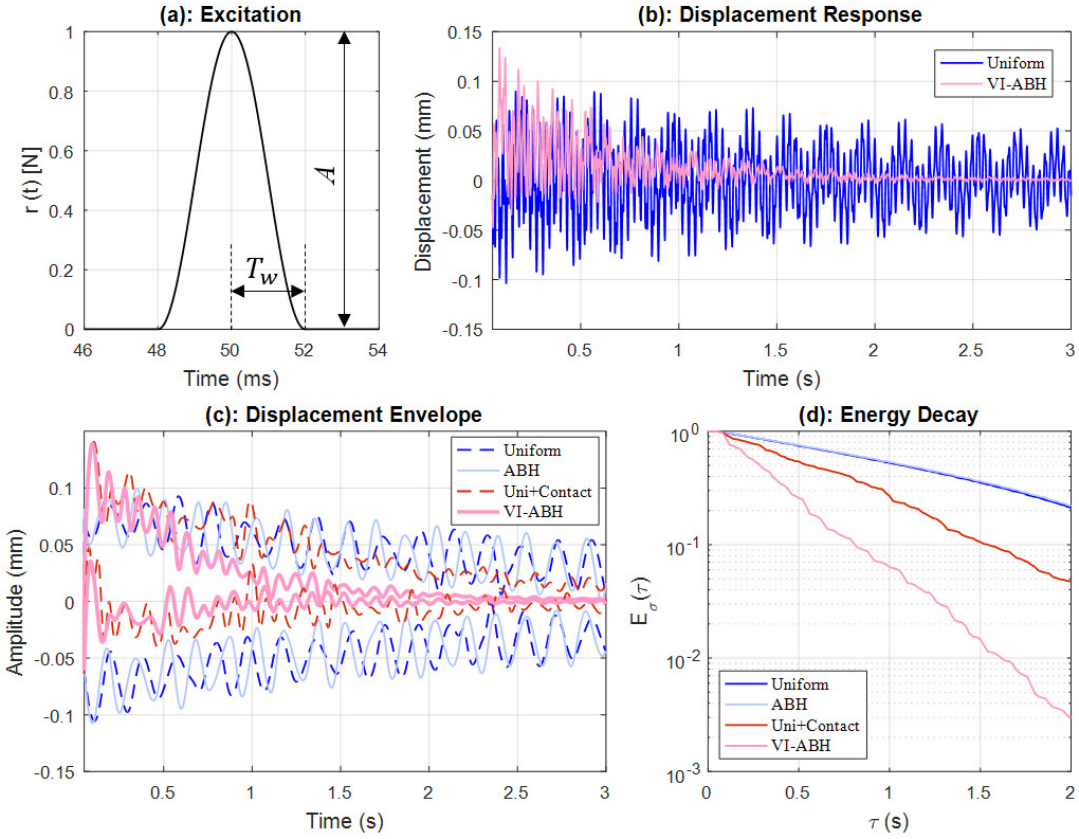

Fig. 12. (a) Temporal content $r(t)$ of the impulse force, having the shape of a raised cosine with amplitude A and temporal width T_w. (b) Displacement of the beam at x_F, comparison between the case of the uniform beam (dark blue) and the VI-ABH (pink). The case of 7 contact points is here investigated, with the contact stiffness as $K_c = 10^7$ N $\cdot$ m$^{-1.5}$. (c) Enveloppe of the displacement curves for four different cases : uniform beam (dashed dark blue), ABH beam (light blue), uniform beam with contact points (dashed red), and VI-ABH with contact points (pink). (d) Energy decay computed from the temporal responses shown in panel (c).

In order to draw out a more quantitative comparison, the energy decay of each of these vibration signals are extracted and compared in Fig. 12(d). The energy decay at a given time $\tau > 0$ is introduced as

$$E_\sigma(\tau) = \frac{\int_\tau^{T_f} w^2 \, \mathrm{d}t}{\int_0^{T_f} w^2 \, \mathrm{d}t}, \quad \forall\, \tau \in [0,\ T_f], \tag{23}$$

where T_f is the total time of the time response and w the displacement of the beam. The numerator of E_σ is homogeneous to the total energy of the displacement signal, and when $\tau = 0$, $E_\sigma = 1$. Increasing the value of τ leads to a decreasing value of E_σ which is represented in Fig. 12(d) for the same four cases. It clearly underlines that the energy decay is almost , with the largest slope obtained for the case of the vibro-impact ABH. The slope of this energy decay will be used hereafter in order to compare quantitatively the relative performances of

different configurations.

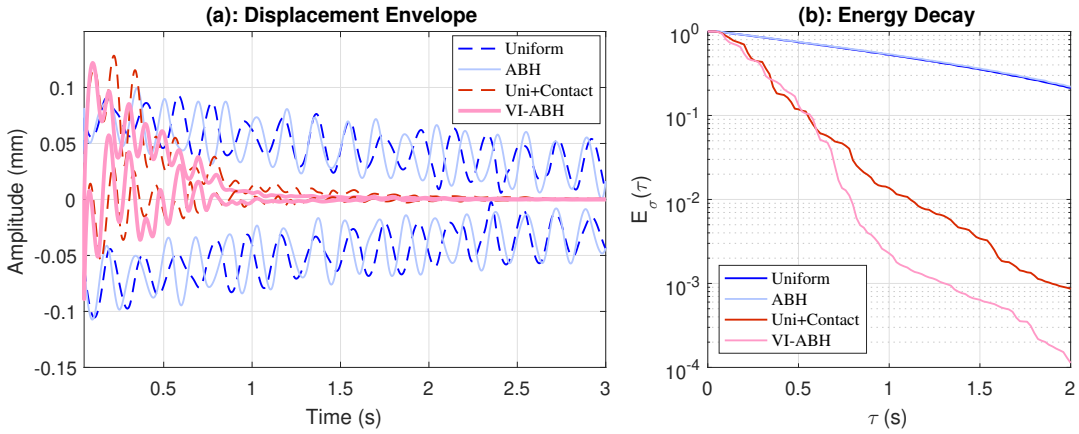

Fig. 13. Transient dynamics under impulsive impact with width $T_w = 2$ ms and amplitude $A = 1$ N, VI-ABH composed of a single contact point at position $x_c = 48$ cm. Stiffness of the contact $K_c = 10^9$ N $\cdot$ m$^{-1.5}$. (a): Envelope of displacements for four different cases. (b): Energy decay following Eq. (23).

Another case of transient response is shown in Fig. 13, for the same excitation but for only one contact point, located at one of the best positions found in Section 3.3, see Fig. 9. More precisely, the contact points is here selected at $x_{c1} = 48$ cm, and a stiffer contact is considered with $K_c = 10^9$ N$\cdot$m$^{-1.5}$. Fig. 13 compares once again the same four cases (uniform beam with and without contact, ABH beam with and without contact). It underlines how the presence of the single contact point is important in order to rapidly damp vibrations, the two curves of beam with contact decreasing very rapidly to zero in less than one second. The energy decay shown in Fig. 13(b) shows that a double decay phenomenon is at hand for the VI-ABH. A first slope allows to reduce the energy down to 10^{-2} in 0.6 seconds, and a second behaviour is observed with an important change of slope, though it occurs once the vibration amplitude is very small.

A parametric study is conducted in order to assess the performance of the different configurations of contact points on the temporal performance in transient regime. For that purpose, the slope of the energy decay curves is extracted by a linear fitting. The values of the slopes for different cases, in dB/s, is used as a quantitative indicator to compare the results. Fig. 14 shows the obtained results when varying the following parameters:

- The number of contact points is increased from 1 to 7, following the rule given by the maximum values of the eigenmode shapes. This will allow to judge the efficacy of using a small or a large number of contact points.

- Two values of the contact stiffness are considered in order to contrast the results with that obtained in previous sections, showing that the larger the contact stiffness is, the better vibration mitigation is obtained, and the lesser contact points are needed.

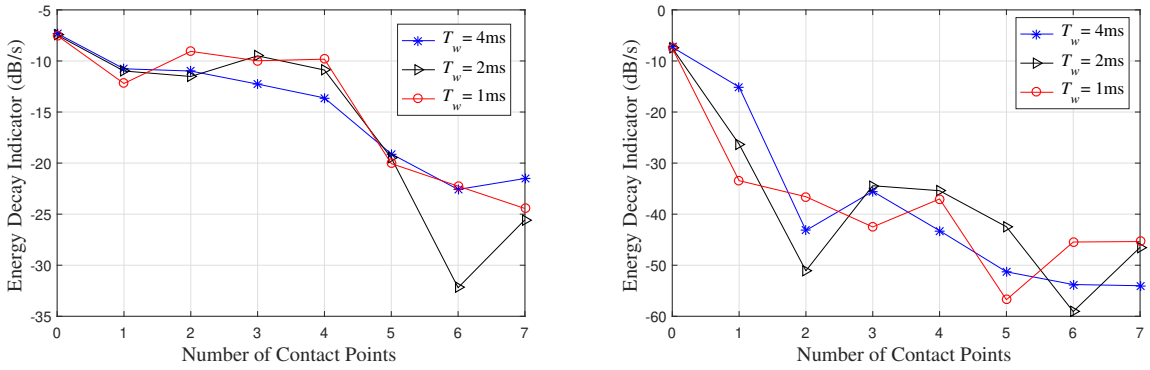

Fig. 14. Energy decay indicator as a function of the number of contact points number, for two different values of the contact stiffness: (a) $K_c = 10^7$ N $\cdot$ m$^{-1.5}$, (b) $K_c = 10^9$ N $\cdot$ m$^{-1.5}$. Three different values of impulse width T_w are compared in each case.

- The input force parameter T_w is also varied in order to verify the mitigation behaviours when varying the frequency band exciting the structure with the initial impulse. Three values are considered: $T_w = 1$ ms (maximum frequency 1000 Hz), $T_w = 2$ ms (maximum frequency 500 Hz) and $T_w = 4$ ms (maximum frequency 250 Hz),

Fig. 14 shows that T_w has a small impact on the damping of vibration, as all the curves have a similar trend in Fig. 14(a) and (b). When the contact is smooth with $K_c = 10^7$ N $\cdot$ m$^{-1.5}$, it is found that increasing the number of contact points have more effect than when the contact is stiff with $K_c = 10^9$ N $\cdot$ m$^{-1.5}$. All these conclusions meet those already derived from the parametric studies led in the permanent regime, showing the robustness of the results found for different excitations.

4. Conclusion

A vibro-impact acoustic black hole (VI-ABH) has been proposed and studied in order to improve the low-frequency efficiency of more traditional acoustic or vibrational back holes, defined as tapered beams with a wedge profile equipped with a visco-elastic layer. The nonlinearity brought by the contact dynamics is used as a way to transfer energy to the high-frequency range where the damping capacity of black holes are much more efficient. By doing so, the nature of the passive damper is significantly modified: the vibrations are strongly nonlinear, with a broadband Fourier spectrum and significant energy in the mid and high frequencies.

The main conclusion that can be drawn from this numerical study is that a valuable improvement can be obtained. In particular, our results show that even without the tapered edge, the damping capacity of a uniform beam is increased by adding a contact nonlinearity in its vibrational behaviour. The conjunction of the vibro-impact nonlinearity with the tapered

profile allows one to obtain concurrent effects, the first one transferring the vibrational energy to the higher frequencies while the second one ensures an optimized passive damping.

Numerical results have shown that the stiffer the contact, the more efficient the energy transfer is, and the better are the improvements in terms of damping capacity. Parametric studies on the optimal locations of contact points also shows that the best strategy is to use the anti-nodes of the low-frequency eigenmodes. Indeed, this method ensures that the resonance peaks of the modes below the cut-on frequency, containing most of the vibrational energy, are broken down. Also, the positive effect of considering bilateral contact points have been clearly underlined.

This study opens the door to other researches on the same topic in order to improve again the device. In particular, larger values of the losses due to the tapered profile (and/or viscoelastic layer) may be seeked in order to obtain more efficiency. Experiments have to be realized for testing the findings of the present study in a real experiment, and coping with experimental limitations. Finally, further numerical studies, for example considering plate models instead of beams, or including geometric nonlinearity, might also be useful in order to fully understand the potentiality of the VI-ABH.

Acknowledgements

This work was realised in IMSIA/ENSTA-Paristech and LAUM, during the one year stay of the first author in France, which was supported by China Scholarship Council (CSC).

Appendix A. Finite difference operators and boundary conditions

Regarding to the operators appearing in Eq. (11), the difference operators $\delta_{\lambda+}$ and $\delta_{\lambda-}$ are defined as

$$\delta_{\lambda+}u = \frac{u_{l+1} - u_l}{\Delta_\lambda}, \tag{A.1}$$

$$\delta_{\lambda-}u = \frac{u_l - u_{l-1}}{\Delta_\lambda}, \tag{A.2}$$

and the averaging operator $\mu_{\lambda-}$ is

$$\mu_{\lambda-}u = \frac{u_l + u_{l-1}}{2}. \tag{A.3}$$

The discrete boundary conditions in Eq. (3) can be expressed as

$$u_0 = u_1 = 0, \tag{A.4}$$

for the clamped boundary condition in $x = 0$, and

$$\delta_{\lambda+}\left(\left(\mu_{\lambda-}\phi^{-1/2}\right)\delta_{\lambda-}u_N\right) = \delta_{\lambda+}\left(\left(\mu_{\lambda-}\phi^{-1/2}\right)\delta_{\lambda-}u_{N-1}\right) = 0, \tag{A.5}$$

for the free boundary condition at $x = L$, respectively.

References

[1] D. Ross, E.E. Ungar, and E.M. Kerwin. Damping of plate flexural vibrations by means of viscoelastic laminae. *Structural damping*, pages 49–97, 1959.

[2] J.P. Den Hartog. *Mechanical Vibrations*. McGraw-Hill, New-York, 1934.

[3] H.C. Tsai and G.C. Lin. Optimum tuned mass dampers for minimizing steady-state response of support excited and damped system. *Earthquake Engineering and Structural Dynamics*, 11:846–862, 1993.

[4] S. Krenk and J. Hogsberg. Tuned mass absorber on a flexible structure. *Journal of Sound and Vibration*, 333:1577–1595, 2014.

[5] M.A. Mironov. Propagation of a flexural wave in a plate whose thickness decreases smoothly to zero in a finite interval, 1988.

[6] V.V. Krylov and F.J.B.S. Tilman. Acoustic black holes for flexural waves as effective vibration dampers. *Journal of Sound and Vibration*, 274(3-5):605–619, 2004.

[7] V.B. Georgiev, J. Cuenca, F. Gautier, L. Simon, and V.V. Krylov. Damping of structural vibrations in beams and elliptical plates using the acoustic black hole effect. *Journal of sound and vibration*, 330(11):2497–2508, 2011.

[8] L. Tang, L. Cheng, H. Ji, and J. Qiu. Characterization of acoustic black hole effect using a one-dimensional fully-coupled and wavelet-decomposed semi-analytical model. *Journal of Sound and Vibration*, 374:172 – 184, 2016.

[9] V. Denis, A. Pelat, F. Gautier, and B. Elie. Modal overlap factor of a beam with an acoustic black hole termination. *Journal of Sound and Vibration*, 333(12):2475–2488, 2014.

[10] D.J. O'Boy, V.V. Krylov, and V. Kralovic. Damping of flexural vibrations in rectangular plates using the acoustic black hole effect. *Journal of Sound and Vibration*, 329(22):4672–4688, 2010.

[11] M.R. Shepherd, C.A. McCormick, S.C. Conlon, and P.A. Feurtado. Modeling and optimization of acoustic black hole vibration absorbers. *The Journal of the Acoustical Society of America*, 141(5):4034–4034, 2017.

[12] L. Tang and L. Cheng. Enhanced acoustic black hole effect in beams with a modified thickness profile and extended platform. *Journal of Sound and Vibration*, 391:116 – 126, 2017.

[13] J. Deng, L. Zheng, P. Zeng, Y. Zuo, and O. Guasch. Passive constrained viscoelastic layers to improve the efficiency of truncated acoustic black holes in beams. *Mechanical Systems and Signal Processing*, 118:461 – 476, 2019.

[14] J. Y. Lee and W. Jeon. Vibration damping using a spiral acoustic black hole. *The Journal of the Acoustical Society of America*, 141(3):1437–1445, 2017.

[15] S.C. Conlon, J.B. Fahnline, and F. Semperlotti. Numerical analysis of the vibroacoustic properties of plates with embedded grids of acoustic black holes. *The Journal of the Acoustical Society of America*, 137(1):447–457, 2015.

[16] L. Zhao, S. C. Conlon, and F. Semperlotti. Broadband energy harvesting using acoustic black hole structural tailoring. *Smart Materials and Structures*, 23(6):065021, 2014.

[17] V.V. Krylov and R.E.T.B. Winward. Experimental investigation of the acoustic black hole effect for flexural waves in tapered plates. *Journal of Sound and Vibration*, 300(1-2):43–49, 2007.

[18] V. Denis, F. Gautier, A. Pelat, and J. Poittevin. Measurement and modelling of the reflection coefficient of an acoustic black hole termination. *Journal of Sound and Vibration*, 349:67–79, 2015.

[19] E.P. Bowyer, D.J. O'Boy, V.V. Krylov, and F. Gautier. Experimental investigation of damping flexural vibrations in plates containing tapered indentations of power-law profile. *Applied Acoustics*, 74(4):553–560, 2013.

[20] E.P. Bowyer, D.J. O'Boy, V.V. Krylov, and J.L. Horner. Effect of geometrical and material imperfections on damping flexural vibrations in plates with attached wedges of power law profile. *Applied Acoustics*, 73(5):514–523, 2012.

[21] P.A. Feurtado and S.C. Conlon. An experimental investigation of acoustic black hole dynamics at low, mid, and high frequencies. *Journal of Vibration and Acoustics*, 138(6):061002, 2016.

[22] O. Aklouche, A. Pelat, S. Maugeais, and F. Gautier. Scattering of flexural waves by a pit of quadratic profile inserted in an infinite thin plate. *Journal of Sound and Vibration*, 375:38–52, 2016.

[23] V. Denis, A. Pelat, C. Touzé, and F. Gautier. Improvement of the acoustic black hole effect by using energy transfer due to geometric nonlinearity. *International Journal of Non-Linear Mechanics*, 94:134–145, 2017.

[24] O. Gendelman, L. I. Manevitch, A. F. Vakakis, and R. M. Closkey. Energy pumping in nonlinear mechanical oscillators, I: dynamics of the underlying Hamiltonian systems. *Journal of Applied Mechanics*, 68(1):34 – 41, 2001.

[25] A. F. Vakakis, L. I. Manevitch, O. Gendelman, and L. Bergman. Dynamics of linear discrete systems connected to local, essentially non–linear attachments. *Journal of Sound and Vibration*, 264:559 – 577, 2003.

[26] A. F. Vakakis, O. V. Gendelman, L. A. Bergman, D. M. McFarland, G. Kerschen, and Y. S. Lee. *Nonlinear Targeted Energy Transfer in Mechanical and Structural Systems*. Springer, series: Solid Mechanics and its Applications. Springer, 2009.

[27] Y.S. Lee, F. Nucera, A.F. Vakakis, D.M. McFarland, and L.A. Bergman. Periodic orbits, damped transitions and targeted energy transfers in oscillators with vibro–impact attachments. *Physica D: Nonlinear Phenomena*, 238(18):1868 – 1896, 2009.

[28] C.H. Lamarque, O.V. Gendelman, A. Ture Savadkoohi, and E. Etcheverria. Targeted energy transfer in mechanical systems by means of non–smooth nonlinear energy sink. *Acta Mechanica*, 221(1 - 2):175 – 200, 2011.

[29] E. Gourc, G. Michon, S. Séguy, and A. Berlioz. Targeted energy transfer under harmonic forcing with a vibro-impact nonlinear energy sink: Analytical and experimental developments. *Journal of Vibration and Acoustics*, 137(3):031008, 2015.

[30] M. A. Al-Shudeifat, A. F. Vakakis, and L. A. Bergman. Shock mitigation by means of low– to high–frequency nonlinear targeted energy transfers in a large–scale structure. *Journal of Computational and Nonlinear Dynamics*, 11(2):021006, 2015.

[31] G. Pennisi, C. Stephan, E. Gourc, and G. Michon. Experimental investigation and analytical description of a vibro–impact NES coupled to a single–degree–of–freedom linear oscillator harmonically forced. *Nonlinear Dynamics*, 88(3):1769 – 1784, 2017.

[32] R.P. Goel. Transverse vibrations of tapered beams. *Journal of Sound and Vibration*, 47(1):1 – 7, 1976.

[33] J. R. Banerjee and F. W. Williams. Exact Bernoulli-Euler dynamic stiffness matrix for a range of tapered beams. *International Journal for Numerical Methods in Engineering*, 21(12):2289–2302, 1985.

[34] R. A. Ibrahim. *Vibro-impact dynamics: modeling, mapping and applications*, volume 43. Springer Science & Business Media, 2009.

[35] S. Bilbao, A. Torin, and V. Chatziioannou. Numerical modeling of collisions in musical instruments. *Acta Acustica united with Acustica*, 101(1):155–173, 2015.

[36] C. Issanchou, S. Bilbao, J.-L Le Carrou, C. Touzé, and O. Doaré. A modal-based approach to the nonlinear vibration of strings against a unilateral obstacle: Simulations and experiments in the pointwise case. *Journal of Sound and Vibration*, 393:229–251, 2017.

[37] W. Goldsmith. *Impact*. Courier Corporation, 2001.

[38] V. Chatziioannou and M. van Walstijn. Energy conserving schemes for the simulation of musical instrument contact dynamics. *Journal of Sound and Vibration*, 339:262–279, 2015.

[39] M. Farid and O.V. Gendelman. Response regimes in equivalent mechanical model of strongly nonlinear liquid sloshing. *International Journal of Non-Linear Mechanics*, 94:146–159, 2017.

[40] K.H. Hunt and F.R.E. Crossley. Coefficient of restitution interpreted as damping in vibroimpact. *Journal of applied mechanics*, 42(2):440–445, 1975.

[41] S. Bilbao. *Numerical sound synthesis: finite difference schemes and simulation in musical acoustics*. John Wiley & Sons, 2009.

[42] M. van Walstijn and J. Bridges. Simulation of distributed contact in string instruments: a modal expansion approach. In *Signal Processing Conference (EUSIPCO), 2016 24th European*, pages 1023–1027. IEEE, 2016.

[43] V. Yastrebov. *Numerical Methods in Contact Mechanics*. Wiley-ISTE, 2013.

[44] B. Brogliato and V. Acary. Numerical methods for nonsmooth dynamical systems. *Lecture Notes in Applied and Computational Mechanics*, 35, 2008.